Editors' Suggestion

Conservation Laws and Slow Dynamics Determine the Universality Class of Interfaces in Active Matter

Raphaël Maire,* Andrea Plati, Frank Smallenburg, and Giuseppe Foffi†
Université Paris-Saclay, CNRS, Laboratoire de Physique des Solides, 91405 Orsay, France

(Received 24 November 2025; revised 27 January 2026; accepted 10 March 2026; published 6 April 2026)

While equilibrium interfaces display universal large-scale statistics, interfaces in phase-separated active and driven systems are predicted to belong to distinct nonequilibrium universality classes. Yet, such behavior has proven difficult to observe, with most systems exhibiting equilibriumlike fluctuations despite their strongly nonequilibrium microscopic dynamics. We introduce a hard-disk model driven by active collisions, conceived as an effective two-dimensional description of a vibrofluidized granular system that, contrary to self-propelled models, displays clear nonequilibrium interfacial scaling. We observe for the first time, the $|\boldsymbol{q}|$KPZ and wet-$|\boldsymbol{q}|$KPZ universality classes while revealing a new, previously overlooked universality class arising in systems with slow solidlike or glassy dynamics. Conservation laws and slow dynamics select these distinct classes.

DOI: 10.1103/b7s9-4l4q

Introduction—At thermodynamic equilibrium, the Boltzmann distribution governs all static observables [1]. For example, every liquid-gas critical point—whether in a colloidal suspension, a molecular fluid, or the μVT ensemble—shares the same static critical exponents [2], while the dynamics are captured by different dynamical exponents z [3,4]. Similarly, interfaces in equilibrium phase-separated systems—such as those found in liquid-liquid colloid demixing [5], polymer blends [6], electrolyte solutions [7], or two-dimensional (2D) Ising models [8]—are all governed by the capillary-wave Hamiltonian on large scales with surface tension γ: $\mathcal{H}[h] \simeq (\gamma/2)\int d^dx(\boldsymbol{\nabla} h)^2$, where $h(\boldsymbol{x},t)$ is the height of a d-dimensional interface [9]. Dynamically, projection methods show that the Fourier components $h(\boldsymbol{k},t)$ evolve as [9–17]

$$\partial_t h(\boldsymbol{k},t) = -\kappa|\boldsymbol{k}|^{\alpha-2}\frac{\delta\mathcal{H}}{\delta h} + \sqrt{2\kappa|\boldsymbol{k}|^{\alpha-2}D}\zeta(\boldsymbol{k},t), \quad (1)$$

where D is proportional to the temperature, $\zeta(\boldsymbol{k},t)$ is a unit-variance Gaussian white noise, and $\kappa|\boldsymbol{k}|^{\alpha-2}$ is a damping. The dynamical exponent z characterizing the interface relaxation time equals α, which depends on the conservation laws of the underlying $(d+1)$-dimensional order parameter dynamics [12]. The fluctuation dissipation theorem ensures that static properties quantified by the static height correlation $S_h(\boldsymbol{k}) \equiv \langle|h(\boldsymbol{k})|^2\rangle \sim \boldsymbol{k}^{-d-2\chi}$ with $\chi = (2-d)/2$ are independent of z at equilibrium [9]. This decoupling between statics and dynamics is, however, only guaranteed at equilibrium.

With the rise of interest in active matter [18–20] and the ubiquity of interfaces in biology [21–27], research on far-from-equilibrium interfaces has surged. In this Letter, we focus not on growing interfaces, such as those described by Kardar-Parisi-Zhang (KPZ) [28,29], which make up a large class of physical systems, but rather on nongrowing interfaces in phase-separated systems. Freed from a Hamiltonian framework, these interfaces can exhibit peculiar behavior such as negative surface tension [20,30–32], instabilities [9,33–36], and traveling waves [37–40]. These effects can typically be captured either by introducing effective parameters into the equilibrium interface equation [Eq. (1)] or by coupling this equation to another field. Surprisingly, the measured fluctuations in granular or scalar active matter interfaces often follow the equilibrium result: $S \sim |\boldsymbol{k}|^{-2}$ [41–52]. This equilibriumlike behavior remains puzzling. While microscopic violations of detailed balance do not always survive coarse graining in other systems [53–60], theoretical predictions for interfaces in active matter suggest a wide variety of nonequilibrium behaviors depending on the conserved quantity of the underlying dynamics. For example, in overdamped systems, such as active Brownian particles, the interface is predicted to obey the $|\boldsymbol{q}|$KPZ equation [61,62],

$$\partial_t h = -\kappa\gamma|\boldsymbol{k}|^3 h + \lambda|\boldsymbol{k}|\mathcal{F}[(\boldsymbol{\nabla} h)^2] + \sqrt{2\kappa|\boldsymbol{k}|D}\zeta, \quad (2)$$

where $\mathcal{F}$ denotes the Fourier transform and λ controls the nonlinearity strength. Despite extensive research in interfacial fluctuations of active matter interfaces [41–48,52], $|\boldsymbol{q}|$KPZ has been reported only once in numerical simulations of strongly confined active particles [63]. Including

*Contact author: raphael.maire@universite-paris-saclay.fr
†Contact author: giuseppe.foffi@universite-paris-saclay.fr

momentum conservation should yield the wet-$|\boldsymbol{q}|$KPZ equation [64],

$$\partial_t h = -\kappa\gamma|\boldsymbol{k}|h + \lambda|\boldsymbol{k}|^{-1}\mathcal{F}[(\boldsymbol{\nabla}h)^2] + \sqrt{2\kappa|\boldsymbol{k}|^{-1}D\zeta}, \quad (3)$$

which remains unobserved. Finally, for some nonequilibrium hyperuniform (HU) systems where the noise is momentum conserving, but the deterministic evolution includes viscous drag so that momentum is not a locally conserved quantity [65–67], the interface obeys

$$\partial_t h = -\kappa\gamma|\boldsymbol{k}|^3 h + \sqrt{2\kappa|\boldsymbol{k}|^2 D\zeta}. \quad (4)$$

To date, only this last equation has been clearly observed numerically in large-scale systems [68]. For 1D interfaces, each of these cases has different exponents:

1D interface	Eq.	χ	z	Ref.
Equilibrium	(1)	1/2	α	[9]
$\|\boldsymbol{q}\|$KPZ	(2)	0.3–0.4	2.2–2.8	[61,64]
Wet $\|\boldsymbol{q}\|$KPZ	(3)	1	1	[64]
HU interface	(4)	0	3	[68]

Thus, three predicted nonequilibrium phase-separating models with distinct dynamics yield different static roughness exponents, breaking equilibrium universality.

The contribution of this Letter is twofold. (i) We introduce a hard-disk model driven by active collisions, inspired by a vibrated granular system which, in contrast to regular self-propelled active matter, exhibits clearly and for the first time all three nonequilibrium universality classes theoretically predicted for interfaces separating coexisting liquid and gas phases. (ii) We show that the emergence of solidlike ordering or glassiness in one of the phases qualitatively modifies interfacial fluctuations, leading to new, previously overlooked universality classes. Taken together, these results reveal how conservation laws and slow relaxation processes can fundamentally reshape the static properties of interfaces in active matter systems.

Model—Taking inspiration from a granular system [69,70], we model N 2D hard disks of mass m and diameter σ in a periodic $L_x \times L_y$ box at packing fraction $\phi = N\pi\sigma^2/(4L_xL_y)$. Each particle i follows the Langevin equation,

$$m\frac{d^2\boldsymbol{r}_i}{dt^2} = -m\Gamma\frac{d\boldsymbol{r}_i}{dt} + \sum_{j\neq i}\boldsymbol{F}_{ij}^{\mathrm{coll}} + \sqrt{2m\Gamma T}\boldsymbol{\zeta}_i(t), \quad (5)$$

where Γ is a damping, T is a kinetic temperature, and $\boldsymbol{F}_{ij}^{\mathrm{coll}}$ acts as a momentum-conserving nonequilibrium collision such that at contact ($|\boldsymbol{r}_i - \boldsymbol{r}_j| = \sigma$), the kinetic energy of i and j changes by [68,71]

$$\Delta E_{ij} = \Delta E_{ij}^{+} - m\frac{1-\alpha^2}{4}(\boldsymbol{v}_{ij}\cdot\hat{\boldsymbol{\sigma}}_{ij})^2, \quad (6)$$

with $\boldsymbol{v}_{ij} = \boldsymbol{v}_i - \boldsymbol{v}_j$, $\hat{\boldsymbol{\sigma}}_{ij} = (\boldsymbol{r}_i - \boldsymbol{r}_j)/|\boldsymbol{r}_i - \boldsymbol{r}_j|$, and $0 \le \alpha \le 1$ a coefficient of restitution. If $\Gamma = 0$, we set $\alpha < 1$ to dissipate the energy injected by $\Delta E_{ij}^{+} > 0$. The injected energy depends on the times since each particle's last collision τ_i and τ_j,

$$\Delta E_{ij}^{+} = 2\delta E_0 + \delta E\left(1 - e^{-\tau_i/\tau_r}\right)^{\beta} + \delta E\left(1 - e^{-\tau_j/\tau_r}\right)^{\beta}, \quad (7)$$

where $2\delta E_0$ and $2(\delta E_0 + \delta E)$ are, respectively, the minimum and maximum possible injected energies. The terms $(1 - e^{-\tau/\tau_r})^{\beta}$ interpolate between these limits: τ_r sets the characteristic recharging time, while β controls how sharp the approach to the maximum is. For large δE, dense regions cool and compress, while dilute regions heat and expand, destabilizing the homogeneous phase and driving phase separation with an interface separating the two phases [68,71]. Physically, Eqs. (6) and (7) provide an effective 2D description of a vibrofluidized granular monolayer: vertical energy injected by a vertically vibrating plate is intermittently converted into horizontal motion during collisions [72]. The eliminated out-of-plane dynamics is encoded as a particle-level internal "recharging" state that controls ΔE_{ij}^{+}. In this coarse-grained 2D picture, the activity emerges through collision-mediated energy transfer, similar to models with nonreciprocal interactions or chiral forces, where detailed balance is broken by interactions [73,74].

We perform hybrid time-stepped and event-driven molecular dynamics simulations [75] of Eqs. (5) and (6) in an elongated box ($L_x > L_y \equiv L$). Time and energy are measured in arbitrary units $\hat{\tau}$ and $\hat{E} = m(\sigma/\hat{\tau})^2/2$, respectively. The system is initialized with a step density profile along x at the coexistence densities of the two phases, and the interface position $h(y,t)$ is tracked over time (see Supplemental Material [76]).

Numerical results—The critical exponents are obtained from correlation functions starting from the flat interface of initial size L at $t = 0$ [79],

$$W^2(L,t) \sim \begin{cases} L^{2\chi} & \text{if } t \gg \tau_{\mathrm{ss}}(L) \\ t^{2\chi/z} & \text{if } t \ll \tau_{\mathrm{ss}}(L) \end{cases}, \qquad \tau_{\mathrm{ss}}(L) \sim L^z, \quad (8)$$

where $W^2 \equiv \langle (h(y,t) - \langle h(y,t)\rangle_L)^2\rangle_L$ is the mean-squared width of the interface and τ_{ss} is the time required to reach stationarity. In practice, we estimate τ_{ss} from the intersection between the early-time fit $W^2 \sim t^{2\chi/z}$ and the saturation value $W^2(L, t\to\infty)$ [76]. We will also use the static height correlation in the steady state $S_h(k) \equiv \langle |h(k, t \gg \tau_{\mathrm{ss}})|^2\rangle_L \sim k^{-1-2\chi}$ in 1D. The simulation results are summarized in Fig. 1, with three limiting cases of our model shown in different rows. The average $\langle\cdot\rangle_L$ is over initial conditions with system size and flat interface length $L_y = L$ and, when applicable, multiple uncorrelated snapshots of the same run.

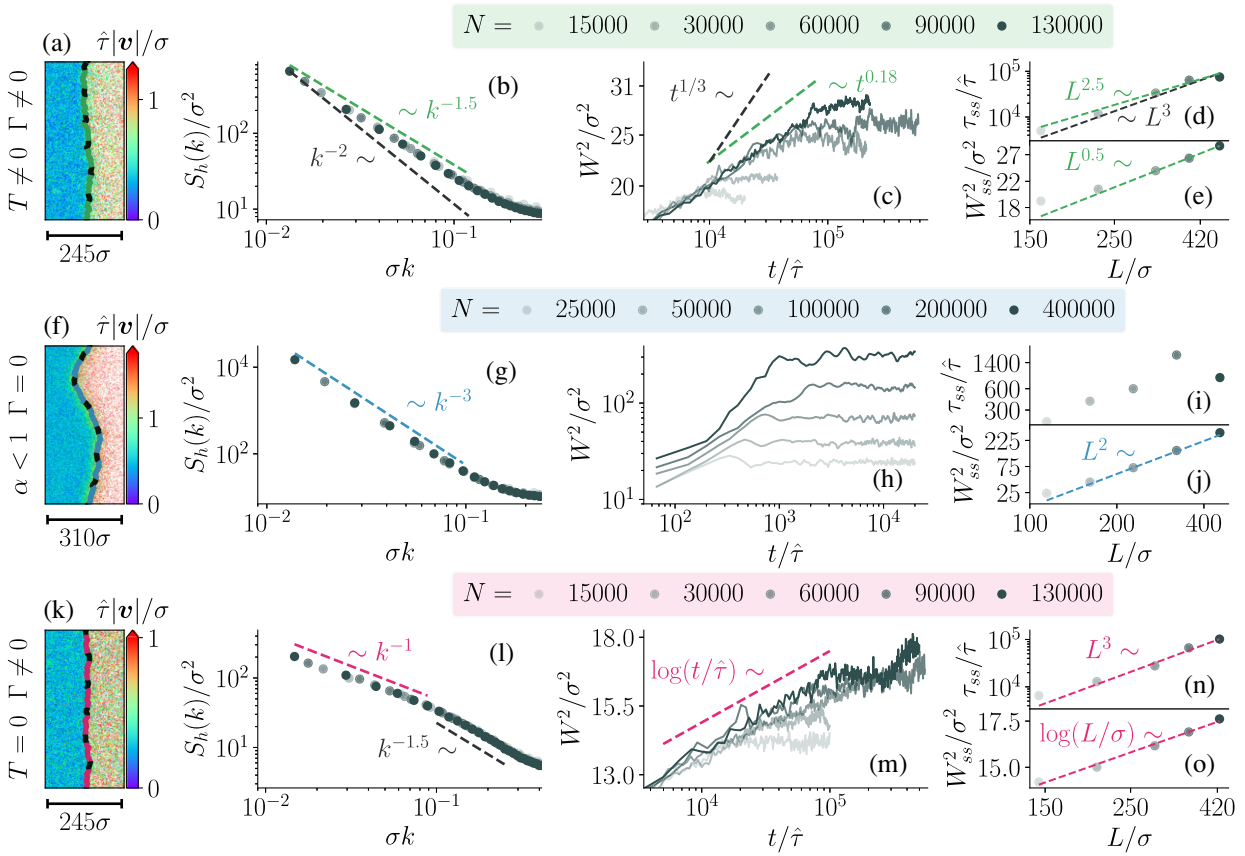

FIG. 1. Simulations of three qualitatively distinct systems based on Eqs. (5) and (6). In the first row, only the density field is conserved; in the second row, momentum is also conserved, and in the last row, only the density field is conserved, but the mesoscopic noise conserves the center of mass of the system. (a),(f),(k) Snapshots centered on the interface, with particles colored by velocity. (b),(g),(l) The steady-state static height correlations as a function of wave number. (c),(h),(m) The time evolution of the interface width squared, starting from a flat interface, for various system sizes. (d),(e),(i),(j),(n),(o) The system-size dependence of the coarsening time and steady-state width squared $W^2_{\rm ss} \equiv W^2(t \to \infty)$. The averages are computed over 50–1000 independent initial configurations, with at least 300 snapshots taken for each configuration. In (a)–(e), we set $T/\hat{E} = 0.05$, $\Gamma/\hat{\tau} = 0.05$, $\tau_r/\hat{\tau} = 4$, $\delta E_0/\hat{E} = 0.0025$, $\delta E/\hat{E} = 15$, $\beta = 10$, $\alpha = 0.99$, and $L_x = 2L_y$. For (f)–(j), we set $\Gamma/\hat{\tau} = 0$, $\tau_r/\hat{\tau} = 3$, $\delta E_0/\hat{E} = 0.0125$, $\delta E/\hat{E} = 25$, $\beta = 10$, $\alpha = 0.95$, and $L_x = 8L_y$. For (k)–(o), we set $T/\hat{E} = 0$, $\Gamma/\hat{\tau} = 0.075$, $\tau_r/\hat{\tau} = 3$, $\delta E_0/\hat{E} = 0.0125$, $\delta E/\hat{E} = 25$, $\beta = 10$, and $\alpha = 0.95$, $L_x = 2L_y$.

(i) $|\boldsymbol{q}|$KPZ scaling. In the top row ($T \neq 0$ and $\Gamma \neq 0$), the Langevin bath damps the momentum, leaving the density as the only conserved field. This should place the resulting interface in the $|\boldsymbol{q}|$KPZ universality class where the following critical exponents are expected: $2.2 \lesssim z^{|\boldsymbol{q}|\text{KPZ}} \lesssim 2.8$ and $0.3 \lesssim \chi^{|\boldsymbol{q}|\text{KPZ}} \lesssim 0.4$. Figure 1(a) shows a snapshot where the dense (left) region is colder, a strong nonequilibrium signature. The interface roughness is quantified in Fig. 1(b) by the static height correlation $S_h(k) \sim k^{-1.5}$, yielding $\chi \simeq 0.25$. This roughness is significantly reduced compared to the equilibrium value $\chi^{\rm eq} = 1/2$. Figure 1(c) presents the time evolution of the interface width squared for various system sizes. During coarsening, we observe a slow growth of the interface width squared $W^2(t) \sim t^{0.18}$, incompatible with the equilibrium scaling $\sim t^{1/3}$. Combining this with $\chi \simeq 0.25$ yields a dynamical exponent $z \simeq 2\chi/0.18 \simeq 2.78$ via Eq. (8). These exponents are confirmed in Figs. 1(d) and 1(e), which show measurement of $\tau_{\rm ss}$ and $W^2_{\rm ss} \equiv W^2(t \to \infty)$ as a function of L. Within finite-size limitations, our measured exponents are therefore consistent with the $|\boldsymbol{q}|$KPZ scaling.

(ii) Wet-$|\boldsymbol{q}|$KPZ scaling. In the middle row ($\Gamma = 0$), the momentum is locally conserved due to the absence of a Langevin bath. This additional conservation law is expected to place the system in the wet-$|\boldsymbol{q}|$KPZ universality class, characterized by $z^{\rm wet} = 1$ and $\chi^{\rm wet} = 1$. As shown in Fig. 1(f), the interface is visibly rougher than in the previous case. This is quantified in Figs. 1(g) and 1(j), where $S_h(k) \sim k^{-3}$ and $W^2_{\rm ss} \sim L^2$ are found, both yielding $\chi \simeq 1$, consistent with theoretical expectations. The dynamics in Figs. 1(h) and 1(i), however, show deviation from standard coarsening behavior: the interface width does not exhibit clear power-law growth. This is consistent with direct simulation of the wet-$|\boldsymbol{q}|$KPZ field equation,

which reported an anomalous roughening [64]. Our simulations are also plagued by persistent oscillations (see Supplemental Material [76]). For these reasons, we do not try to investigate the typical coarsening time of this system.

(iii) Hyperuniform scaling. In the bottom row ($T = 0$ and $\Gamma \neq 0$), momentum is damped but still conserved by the collisions—the only source of activity. As shown in Fig. 1(k), this leads to a very flat interface [68]. This is quantified in Fig. 1(l), where the static height correlation scales as $S_h(k) \sim k^{-1}$, consistent with the theoretical prediction $\chi^{\mathrm{HU}} = 0$ in $d = 1$. $\chi = 0$ implies that the interface width grows only logarithmically during coarsening [Fig. 1(m)], preventing a meaningful extraction of z from early-time dynamics. Instead, we determine z from the relaxation time [Fig. 1(n)], obtaining $z \simeq 3$, in agreement with the theoretical prediction $z^{\mathrm{HU}} = 3$. Finally, Fig. 1(o) further confirms the vanishing roughness exponent, $\chi = 0$.

Liquid-solid interfaces—Having identified three universality classes for nonequilibrium liquid-gas interfaces, we now turn to nonequilibrium solid-liquid interfaces that often arise in active matter [80–84]. While equilibrium 1D solid-liquid interfaces exhibit capillary-wave-like behavior [85], out of equilibrium, the slow relaxation of the bulk may modify the interface's static exponents.

A hexagonal ordering naturally emerges when the dense phase exceeds a packing fraction $\phi \gtrsim 0.7$, yielding either a hexatic or a solid phase. Such a high packing fraction can be induced by tuning parameters ($\alpha \to 0$ or $\delta E_0 \to 0$) to make the dense phase effectively colder, promoting a tightly packed phase. Figure 2 presents simulations of

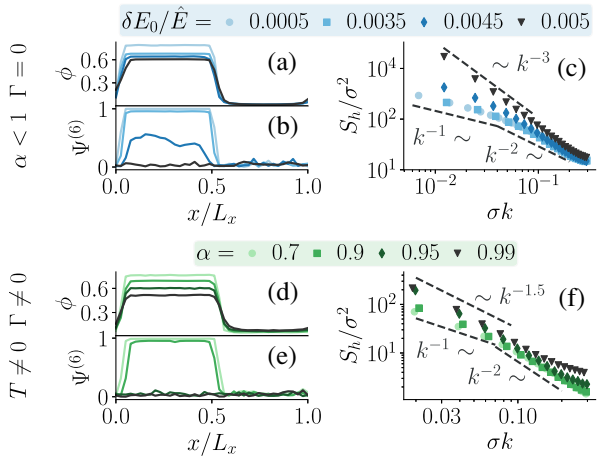

FIG. 2. Simulations of a liquid-solid interface in a system with momentum conservation (top) and without momentum conservation (bottom). (a),(d) The local packing fraction and (b), (e) bond-orientational order profiles normal to the interface. (c),(f) The static height correlations with respect to the wave vector, showing a scaling change when the dense phase undergoes a structural change. The parameters, except the ones explicitly varied, are the same as in Fig. 1. For the system with $\Gamma = 0$, $N \simeq 2 \times 10^5$, for the other $N \simeq 8 \times 10^4$.

liquid-solid interfaces, focusing on their static properties (coarsening dynamics and finite-size analysis are detailed in Supplemental Material [76]). The top row corresponds to momentum-conserving systems at various δE_0, where wet-$|\boldsymbol{q}|$KPZ scaling is expected for liquid-gas interfaces. Figure 2(a) shows the local packing fraction profile in the direction normal to the interface. As expected, lowering δE_0 increases the dense phase packing. In Fig. 2(b), we quantify the hexagonal-like ordering using the bond-orientational order parameter, defined for each particle i as $\psi_i^{(6)} = N_i^{-1} \sum_j e^{i6\theta_{ij}}$, where N_i is the number of neighbors of i and θ_{ij} is the angle between particle i, its neighbors j (with $|\boldsymbol{r}_i - \boldsymbol{r}_j| < 1.3\sigma$), and an arbitrary reference axis. At low δE_0, $\Psi^{(6)} = N^{-1} |\sum_i \psi_i^{(6)}| \to 1$, indicating a well-ordered hexagonal packing on these scales. At higher δE_0, the system remains disordered, and $\Psi^{(6)}$ remains small. For the intermediate case ($\delta E_0/\hat{E} = 0.0045$), the average bond-orientational parameter is reduced because contributions from slowly coarsening multiple hexatic domains partially cancel one another. In Fig. 2(c), we show the interface fluctuations for these various systems. As expected, the system with a liquid dense phase follows the wet-$|\boldsymbol{q}|$KPZ scaling $\chi \simeq 1$, but as the dense phase orders, the spectrum shifts toward $\chi \simeq 0$. In the bottom row of Fig. 2, we perform the same analysis but for a system without momentum conservation. As shown in Fig. 2(f), when the system orders [for $\alpha \leq 0.9$, as seen in Figs. 2(d) and 2(e)], the static height correlations deviate from the expected $|\boldsymbol{q}|$KPZ scaling and $\chi \to 0$. This qualitatively mirrors the behavior observed in the momentum-conserving system. The system with center-of-mass conservation is also found to remain at $\chi = 0$. Thus, the change of structure in the dense phase coincides with a universal shift of χ from its liquid-gas value to 0.

Liquid-glass interfaces—We now analyze liquid-glass interfaces, which are highly relevant in biological systems [86–89]. Similar to solids, the dynamical arrest of glasses and their low-energy excitations [90–92] may influence the static scaling of nonequilibrium interfaces. To suppress crystallinelike structures and enable liquid-glass coexistence, we replace the monodisperse system with an equimolar binary mixture of large and small hard particles of size ratio 0.7, both governed by the same equations of motion [76]. Denser phases are accessed by reducing the minimum injected energy $2\delta E_0$. Simulations for a momentum-conserving system are presented in Fig. 3(a). At high δE_0, the scaling exponent $\chi^{\mathrm{wet}} = 1$ is recovered, as expected for an interface separating liquid and gas phases. However, as δE_0 is reduced, the dense phase undergoes dynamical arrest, evidenced by the plateau in the mean-square displacement (inset). This coincides with a decrease of χ from 1 to 0.25. A more stable glass might yield a smaller χ, potentially closer to the value found for the liquid-solid interface. As expected, the resulting

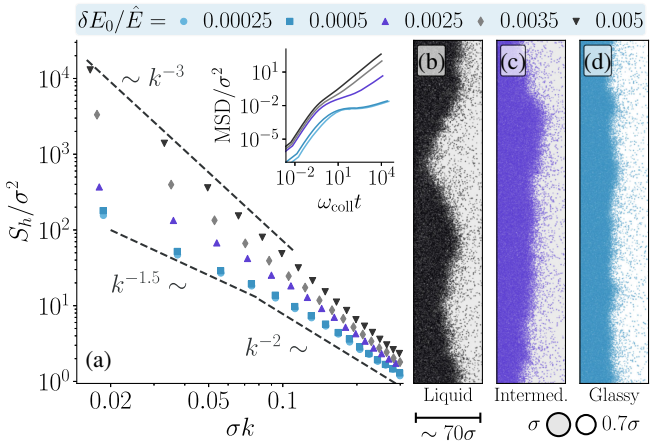

FIG. 3. Simulations of a liquid-glass interface in a binary hard-disk mixture with momentum conservation. (a) Static height correlations versus wave vector show a change in scaling as the dense phase becomes glassy, as measured in the inset showing the mean-square displacement (MSD) of homogeneous systems at the corresponding dense phase densities, plotted against time normalized by the collision rate $\omega_{\rm coll}$. (b)–(d) Representative interface profiles for low, intermediate, and high δE_0. All parameters match those in Fig. 1, except for the varied δE_0 and $\alpha = 0.9$. $2.5 \times 10^5 \leq N \leq 3.5 \times 10^5$. The mixture is equimolar with a size ratio of 0.7, and σ refers to the large particle diameter.

liquid-glass interface is visually less rough than the liquid-gas interface, with typical configurations shown in Figs. 3(b)–3(d). We thus find a phenomenology consistent with that observed for liquid-solid interfaces: the interface roughness decreases when slow dynamics develop in the bulk of the dense phase. For both models, diffusion may be restored in the bulk of the dense phase on large timescales, potentially recovering standard liquid-gas scaling at very small $\boldsymbol{k}$.

Conclusion—We introduced a minimal hard-disk model driven by active collisions that realizes three distinct nonequilibrium liquid-gas universality classes of interfacial fluctuations, each tied to specific bulk conservation laws. We also uncovered that slow dynamics arising from solid-like ordering or glassiness in the denser phase can modify the interface properties. This model directly maps onto quasi-2D vibrated granular systems undergoing phase separation, offering an experimentally accessible platform for probing nonequilibrium interfacial physics [70]. Unlike many active matter systems—where long persistence lengths and interfacial polarization might necessitate a large system to observe universal scaling [93–96]—this granular system may offer a more accessible path to asymptotic behavior.

To go beyond our studies, it would be valuable to develop a theory that predicts the new measured interfacial exponents and that would relate them to the slow relaxation of the bulk. Notably, it would be interesting to determine how the large-scale scaling of the interface is affected when bulk diffusion is restored at long length scales, either by defects in the solid or by the weak stability of the glass. Building on the 1D flat interfaces studied here, exploring two-dimensional or curved interfaces—relevant for biological systems [24–27,97–100], finite-size effects [41], and nucleation [101–105]—offers an interesting direction. For example, nucleation driven by active collisions may exhibit strong nonequilibrium behavior [106], distinct from that in conventional active matter [101]. More generally, interfaces with additional internal order (nematic, smectic, or polar) could reveal new universality classes, offering an exciting avenue for future study.

Acknowledgments—We gratefully acknowledge insightful discussions with Ludovic Berthier and Leonardo Galliano, as well as valuable exchanges with Adhvik Jaghannatan, Lila Sarfati, Julien Tailleur, Cesare Nardini, and Ananyo Maitra.

Data availability—The data that support the findings of this article are not publicly available upon publication because it is not technically feasible and/or the cost of preparing, depositing, and hosting the data would be prohibitive within the terms of this research project. The data are available from the authors upon reasonable request.

[1] M. Kardar, *Statistical Physics of Fields* (Cambridge University Press, Cambridge, England, 2007).
[2] N. Goldenfeld, *Lectures on Phase Transitions and the Renormalization Group* (CRC Press, Boca Raton, 2018).
[3] G. Mazenko, *Nonequilibrium Statistical Mechanics* (John Wiley & Sons, New York, 2006).
[4] U. C. Täuber, *Critical Dynamics: A Field Theory Approach to Equilibrium and Non-Equilibrium Scaling Behavior* (Cambridge University Press, Cambridge, England, 2014).
[5] D. G. Aarts, M. Schmidt, and H. N. Lekkerkerker, Direct visual observation of thermal capillary waves, Science **304**, 847 (2004).
[6] D. Langevin, Light scattering by liquid surfaces, new developments, Adv. Colloid Interface Sci. **289**, 102368 (2021).
[7] M. Safouane and D. Langevin, Surface viscoelasticity of concentrated salt solutions: Specific ion effects, Chem. Phys. Chem. **10**, 222 (2009).
[8] G. Gallavotti, The phase separation line in the two-dimensional Ising model, Commun. Math. Phys. **27**, 103 (1972).
[9] A. Onuki, *Phase Transition Dynamics* (Cambridge University Press, Cambridge, England, 2002).
[10] K. Kawasaki and T. Ohta, Kinetic drumhead model of interface. I, Prog. Theor. Phys. **67**, 147 (1982).
[11] R. I. Slavchov, B. Peychev, and A. S. Ismail, Characterization of capillary waves: A review and a new optical method, Phys. Fluids **33**, 101303 (2021).

[12] A. J. Bray, A. Cavagna, and Rui D. M. Travasso, Interface fluctuations, burgers equations, and coarsening under shear, Phys. Rev. E **65**, 016104 (2001).
[13] R. Bausch, V. Dohm, H. K. Janssen, and R. K. P. Zia, Critical dynamics of an interface in $1+\varepsilon$ dimensions, Phys. Rev. Lett. **47**, 1837 (1981).
[14] R. Zia, Normal coordinates and curvature terms in an interface Hamiltonian, Nucl. Phys. **B251**, 676 (1985).
[15] R. Zia, R. Bausch, H. Janssen, and V. Dohm, Dynamics of an interface coupled to a diffusive bulk mode, Mod. Phys. Lett. B **02**, 961 (1988).
[16] J. Romano, R. Golestanian, and B. Mahault, Dynamics of phase-separated interfaces in inhomogeneous and driven mixtures, Soft Matter **21**, 9245 (2025).
[17] N. Caballero, E. Agoritsas, V. Lecomte, and T. Giamarchi, From bulk descriptions to emergent interfaces: Connecting the Ginzburg-Landau and elastic-line models, Phys. Rev. B **102**, 104204 (2020).
[18] M. Te Vrugt and R. Wittkowski, Metareview: A survey of active matter reviews, Eur. Phys. J. E **48**, 12 (2025).
[19] M. C. Marchetti, J.-F. Joanny, S. Ramaswamy, T. B. Liverpool, J. Prost, M. Rao, and R. A. Simha, Hydrodynamics of soft active matter, Rev. Mod. Phys. **85**, 1143 (2013).
[20] M. E. Cates and C. Nardini, Active phase separation: New phenomenology from non-equilibrium physics, Rep. Prog. Phys. **88**, 056601 (2025).
[21] R. A. Foty and M. S. Steinberg, The differential adhesion hypothesis: A direct evaluation, Dev. Biol. **278**, 255 (2005).
[22] A. A. Hyman, C. A. Weber, and F. Jülicher, Liquid-liquid phase separation in biology, Annu. Rev. Cell Dev. Biol. **30**, 39 (2014).
[23] S. C. Kammeraat, Y.-E. Keta, P. Appleton, I. P. Newton, T. B. Liverpool, R. Sknepnek, I. Näthke, and S. Henkes, Correlated cell movements drive epithelial finger formation, arXiv:2508.01046.
[24] B. Schamberger, R. Ziege, K. Anselme, M. Ben Amar, M. Bykowski, A. P. Castro, A. Cipitria, R. A. Coles, R. Dimova, M. Eder *et al.*, Curvature in biological systems: Its quantification, emergence, and implications across the scales, Adv. Mater. **35**, 2206110 (2023).
[25] B. R. Sabari, A. Dall'Agnese, and R. A. Young, Biomolecular condensates in the nucleus, Trends Biochem. Sci. **45**, 961 (2020).
[26] C. P. Brangwynne, C. R. Eckmann, D. S. Courson, A. Rybarska, C. Hoege, J. Gharakhani, F. Jülicher, and A. A. Hyman, Germline p granules are liquid droplets that localize by controlled dissolution/condensation, Science **324**, 1729 (2009).
[27] A. Molliex, J. Temirov, J. Lee, M. Coughlin, A. P. Kanagaraj, H. J. Kim, T. Mittag, and J. P. Taylor, Phase separation by low complexity domains promotes stress granule assembly and drives pathological fibrillization, Cell **163**, 123 (2015).
[28] M. Kardar, G. Parisi, and Y.-C. Zhang, Dynamic scaling of growing interfaces, Phys. Rev. Lett. **56**, 889 (1986).
[29] K. A. Takeuchi and M. Sano, Universal fluctuations of growing interfaces: Evidence in turbulent liquid crystals, Phys. Rev. Lett. **104**, 230601 (2010).
[30] J. Bialké, J. T. Siebert, H. Löwen, and T. Speck, Negative interfacial tension in phase-separated active Brownian particles, Phys. Rev. Lett. **115**, 098301 (2015).
[31] G. Fausti, E. Tjhung, M. E. Cates, and C. Nardini, Capillary interfacial tension in active phase separation, Phys. Rev. Lett. **127**, 068001 (2021).
[32] R. Singh and M. E. Cates, Hydrodynamically interrupted droplet growth in scalar active matter, Phys. Rev. Lett. **123**, 148005 (2019).
[33] L. Zhao, P. Gulati, F. Caballero, I. Kolvin, R. Adkins, M. C. Marchetti, and Z. Dogic, Asymmetric fluctuations and self-folding of active interfaces, Proc. Natl. Acad. Sci. U.S.A. **121** (2024).
[34] R. Alert, Fingering instability of active nematic droplets, J. Phys. A **55**, 234009 (2022).
[35] R. Adkins, I. Kolvin, Z. You, S. Witthaus, M. C. Marchetti, and Z. Dogic, Dynamics of active liquid interfaces, Science **377**, 768 (2022).
[36] A. Martínez-Calvo, C. Trenado-Yuste, H. Lee, J. Gore, N. S. Wingreen, and S. S. Datta, Interfacial morphodynamics of proliferating microbial communities, Phys. Rev. X **15**, 011016 (2025).
[37] P. Gulati, F. Caballero, I. Kolvin, Z. You, and M. C. Marchetti, Traveling waves at the surface of active liquid crystals, Soft Matter **20**, 7703 (2024).
[38] P. Barthelet and F. Charru, Benjamin-Feir and Eckhaus instabilities with Galilean invariance: The case of interfacial waves in viscous shear flows, Eur. J. Mech.-B **17**, 1 (1998).
[39] L. Langford and A. K. Omar, Phase separation, capillarity, and odd-surface flows in chiral active matter, Phys. Rev. Lett. **134**, 068301 (2025).
[40] F. Raßhofer, S. Bauer, A. Ziepke, I. Maryshev, and E. Frey, Capillary wave formation in conserved active emulsions, arXiv:2505.20028.
[41] L.-H. Luu, G. Castillo, N. Mujica, and R. Soto, Capillary like fluctuations of a solid-liquid interface in a noncohesive granular system, Phys. Rev. E **87**, 040202(R) (2013).
[42] L. Yao and R. L. Jack, Interfacial and density fluctuations in a lattice model of motility-induced phase separation, J. Chem. Phys. **162**, 114902 (2025).
[43] A. Wysocki, R. G. Winkler, and G. Gompper, Propagating interfaces in mixtures of active and passive Brownian particles, New J. Phys. **18**, 123030 (2016).
[44] L. Langford and A. K. Omar, Theory of capillary tension and interfacial dynamics of motility-induced phases, Phys. Rev. E **110**, 054604 (2024).
[45] A. Patch, D. M. Sussman, D. Yllanes, and M. C. Marchetti, Curvature-dependent tension and tangential flows at the interface of motility-induced phases, Soft Matter **14**, 7435 (2018).
[46] C. F. Lee, Interface stability, interface fluctuations, and the Gibbs–Thomson relationship in motility-induced phase separations, Soft Matter **13**, 376 (2017).
[47] S. Paliwal, V. Prymidis, L. Filion, and M. Dijkstra, Non-equilibrium surface tension of the vapour-liquid interface of active Lennard-Jones particles, J. Chem. Phys. **147**, 084902 (2017).
[48] C. Del Junco and S. Vaikuntanathan, Interface height fluctuations and surface tension of driven liquids with

time-dependent dynamics, J. Chem. Phys. **150**, 094708 (2019).
[49] Z. Sun, L. Li, F. Ye, and M. Yang, Interfacial stability in tensionless phase-separated quorum-sensing systems, arXiv:2507.15030.
[50] A. E. Patteson, A. Gopinath, and P. E. Arratia, The propagation of active-passive interfaces in bacterial swarms, Nat. Commun. **9**, 5373 (2018).
[51] R. C. Coelho, N. A. Araújo, and M. M. T. da Gama, Propagation of active nematic–isotropic interfaces on substrates, Soft Matter **16**, 4256 (2020).
[52] E. Chacón, F. Alarcón, J. Ramírez, P. Tarazona, and C. Valeriani, Intrinsic structure perspective for MIPS interfaces in two-dimensional systems of active Brownian particles, Soft Matter **18**, 2646 (2022).
[53] G. G. Lorenzana, D. Martin, Y. Avni, D. S. Seara, M. Fruchart, G. Biroli, and V. Vitelli, When is nonreciprocity relevant?, arXiv:2509.17972.
[54] N. Papanikolaou and T. Speck, Dynamic renormalization of scalar active field theories, arXiv:2404.09999.
[55] F. Caballero and M. E. Cates, Stealth entropy production in active field theories near Ising critical points, Phys. Rev. Lett. **124**, 240604 (2020).
[56] J. O'Byrne, Y. Kafri, J. Tailleur, and F. van Wijland, Time irreversibility in active matter, from micro to macro, Nat. Rev. Phys. **4**, 167 (2022).
[57] A. Plati, R. Maire, F. Boulogne, F. Restagno, F. Smallenburg, and G. Foffi, Self-assembly and non-equilibrium phase coexistence in a binary granular mixture, J. Chem. Phys. **163** (2025).
[58] A. Crisanti, A. Puglisi, and D. Villamaina, Nonequilibrium and information: The role of cross correlations, Phys. Rev. E **85**, 061127 (2012).
[59] É. Fodor, R. L. Jack, and M. E. Cates, Irreversibility and biased ensembles in active matter: Insights from stochastic thermodynamics, Annu. Rev. Condens. Matter Phys. **13**, 215 (2022).
[60] D. Lucente, A. Baldassarri, A. Puglisi, A. Vulpiani, and M. Viale, Inference of time irreversibility from incomplete information: Linear systems and its pitfalls, Phys. Rev. Res. **4**, 043103 (2022).
[61] M. Besse, G. Fausti, M. E. Cates, B. Delamotte, and C. Nardini, Interface roughening in nonequilibrium phase-separated systems, Phys. Rev. Lett. **130**, 187102 (2023).
[62] J. Toner, Roughening of two-dimensional interfaces in nonequilibrium phase-separated systems, Phys. Rev. E **107**, 044801 (2023).
[63] B. Krishan, Finite size scaling and universality classes of one-dimensional active matter interface, Europhys. Lett. **150**, 37003 (2025).
[64] F. Caballero, A. Maitra, and C. Nardini, Interface dynamics of wet active systems, Phys. Rev. Lett. **134**, 087105 (2025).
[65] R. Maire and L. Chaix, Hyperuniformity and conservation laws in non-equilibrium systems, J. Chem. Phys. **163**, 214507 (2025).
[66] D. Hexner and D. Levine, Noise, diffusion, and hyperuniformity, Phys. Rev. Lett. **118**, 020601 (2017).
[67] Y. Lei and R. Ni, Non-equilibrium dynamic hyperuniform states, J. Phys. Condens. Matter **37**, 023004 (2024).
[68] R. Maire, L. Galliano, A. Plati, and L. Berthier, Hyperuniform interfaces in non-equilibrium phase coexistence, Phys. Rev. Lett. **135**, 227102 (2025).
[69] R. Maire, A. Plati, F. Smallenburg, and G. Foffi, Non-equilibrium coexistence between a fluid and a hotter or colder crystal of granular hard disks, J. Chem. Phys. **162**, 124901 (2025).
[70] R. Maire, A. Plati, F. Smallenburg, and G. Foffi, Dynamical and structural properties of an absorbing phase transition: A case study from granular systems, J. Stat. Mech. (2025) 123206.
[71] D. Risso, R. Soto, and M. Guzmán, Effective two-dimensional model for granular matter with phase separation, Phys. Rev. E **98**, 022901 (2018).
[72] R. Brito, D. Risso, and R. Soto, Hydrodynamic modes in a confined granular fluid, Phys. Rev. E **87**, 022209 (2013).
[73] L. Caprini and U. Marini Bettolo Marconi, Bubble phase induced by odd interactions in chiral systems, J. Chem. Phys. **162** (2025).
[74] V. Ouazan-Reboul, J. Agudo-Canalejo, and R. Golestanian, Self-organization of primitive metabolic cycles due to non-reciprocal interactions, Nat. Commun. **14** (2023).
[75] F. Smallenburg, Efficient event-driven simulations of hard spheres, Eur. Phys. J. E **45**, 22 (2022).
[76] See Supplemental Material at http://link.aps.org/supplemental/10.1103/b7s9-4l4q, which includes details on the numerical simulations and the coarsening analysis of the liquid-solid interfaces, which includes Refs. [77,78].
[77] L. Ma, X. Li, and C. Liu, Fluctuation-dissipation theorem consistent approximation of the Langevin dynamics model, Commun. Math. Sci. **15**, 1171 (2017).
[78] F. Smallenburg, G. Del Monte, M. de Jager, and L. Filion, A simple and accurate method to determine fluid–crystal phase boundaries from direct coexistence simulations, J. Chem. Phys. **160**, 224109 (2024).
[79] F. Caballero, C. Nardini, F. van Wijland, and M. E. Cates, Strong coupling in conserved surface roughening: A new universality class?, Phys. Rev. Lett. **121**, 020601 (2018).
[80] A. K. Omar, K. Klymko, T. GrandPre, and P. L. Geissler, Phase diagram of active Brownian spheres: Crystallization and the metastability of motility-induced phase separation, Phys. Rev. Lett. **126**, 188002 (2021).
[81] D. Evans and A. K. Omar, Theory of nonequilibrium crystallization and the phase diagram of active Brownian spheres, arXiv:2411.14536.
[82] L. Caprini, D. Breoni, A. Ldov, C. Scholz, and H. Löwen, Dynamical clustering and wetting phenomena in inertial active matter, Commun. Phys. **7**, 343 (2024).
[83] J. Bialké, T. Speck, and H. Löwen, Active colloidal suspensions: Clustering and phase behavior, J. Non-Cryst. Solids **407**, 367 (2015).
[84] P. Digregorio, D. Levis, A. Suma, L. F. Cugliandolo, G. Gonnella, and I. Pagonabarraga, Full phase diagram of active Brownian disks: From melting to motility-induced phase separation, Phys. Rev. Lett. **121**, 098003 (2018).
[85] S. Safran, *Statistical Thermodynamics of Surfaces, Interfaces, and Membranes* (CRC Press, Boca Raton, 2018).
[86] W. Kang, J. Ferruzzi, C.-P. Spatarelu, Y. L. Han, Y. Sharma, S. A. Koehler, J. A. Mitchel, A. Khan, J. P. Butler, D. Roblyer *et al.*, A novel jamming phase diagram links

tumor invasion to non-equilibrium phase separation, Iscience **24** (2021).
[87] B. R. Parry, I. V. Surovtsev, M. T. Cabeen, C. S. O'hern, E. R. Dufresne, and C. Jacobs-Wagner, The bacterial cytoplasm has glass-like properties and is fluidized by metabolic activity, Cell **156**, 183 (2014).
[88] A. Mongera, P. Rowghanian, H. J. Gustafson, E. Shelton, D. A. Kealhofer, E. K. Carn, F. Serwane, A. A. Lucio, J. Giammona, and O. Campàs, A fluid-to-solid jamming transition underlies vertebrate body axis elongation, Nature (London) **561**, 401 (2018).
[89] S. Sadhukhan, S. Dey, S. Karmakar, and S. K. Nandi, A perspective on active glassy dynamics in biological systems, Eur. Phys. J. Special Topics **233**, 3193 (2024).
[90] P. M. Goldbart, Statistical field theory of equilibrium amorphous solids and the intrinsic heterogeneity distributions that characterize them, arXiv:2505.14954.
[91] L. Gartner and E. Lerner, Nonlinear modes disentangle glassy and goldstone modes in structural glasses, SciPost Phys. **1**, 016 (2016).
[92] Y.-C. Hu and H. Tanaka, Origin of the boson peak in amorphous solids, Nat. Phys. **18**, 669 (2022).
[93] P. Pérez-Bastías and R. Soto, Two-field theory for phase coexistence of active Brownian particles, Phys. Rev. E **112**, 055403 (2025).
[94] L. Caprini, U. Marini Bettolo Marconi, and A. Puglisi, Spontaneous velocity alignment in motility-induced phase separation, Phys. Rev. Lett. **124**, 078001 (2020).
[95] C. F. Lee, Active particles under confinement: Aggregation at the wall and gradient formation inside a channel, New J. Phys. **15**, 055007 (2013).
[96] S. Hermann and M. Schmidt, Active interface polarization as a state function, Phys. Rev. Res. **2**, 022003(R) (2020).
[97] Y. Kuroda, T. Kawasaki, and A. M. Menzel, Effects of curvature on growing films of microorganisms, Biophys. J. **124**, 1609 (2025).
[98] S. Hyde, Z. Blum, T. Landh, S. Lidin, B. Ninham, S. Andersson, and K. Larsson, *The Language of Shape: The Role of Curvature in Condensed Matter: Physics, Chemistry and Biology* (Elsevier, New York, 1996).
[99] C. Liu, D. Cao, S. Liu, and Y. Wu, Nonequilibrium dynamics of membraneless active droplets, arXiv:2511.04181.
[100] D. Zwicker, O. Paulin, and C. Ter Burg, Physics of droplet regulation in biological cells, Rep. Prog. Phys. **88**, 116601 (2025).
[101] M. E. Cates and C. Nardini, Classical nucleation theory for active fluid phase separation, Phys. Rev. Lett. **130**, 098203 (2023).
[102] L. Langford and A. K. Omar, The mechanics of nucleation and growth and the surface tensions of active matter, J. Chem. Phys. **163**, 064901 (2025).
[103] R. Zakine, E. Simonnet, and E. Vanden-Eijnden, Unveiling the phase diagram and reaction paths of the active model b with the deep minimum action method, Phys. Rev. Lett. **133**, 038301 (2024).
[104] D. Richard, H. Löwen, and T. Speck, Nucleation pathway and kinetics of phase-separating active Brownian particles, Soft Matter **12**, 5257 (2016).
[105] N. A. Sarma, D. A. King, X. Wu, B. A. Helms, P. D. Ashby, T. P. Russell, and A. K. Omar, Dynamic permeability in metastable droplet interfacial bilayers, arXiv:2511.09510.
[106] R. Maire, Hyperuniformity in active fluids reshape nucleation and capillary-wave dynamics, arXiv:2602.20308.

Supplementary Material

Raphaël Maire,[1,*] Andrea Plati,[1] Frank Smallenburg,[1] and Giuseppe Foffi[1,†]

[1] *Université Paris-Saclay, CNRS, Laboratoire de Physique des Solides, 91405 Orsay, France*

(Dated: March 10, 2026)

SIMULATION METHODS

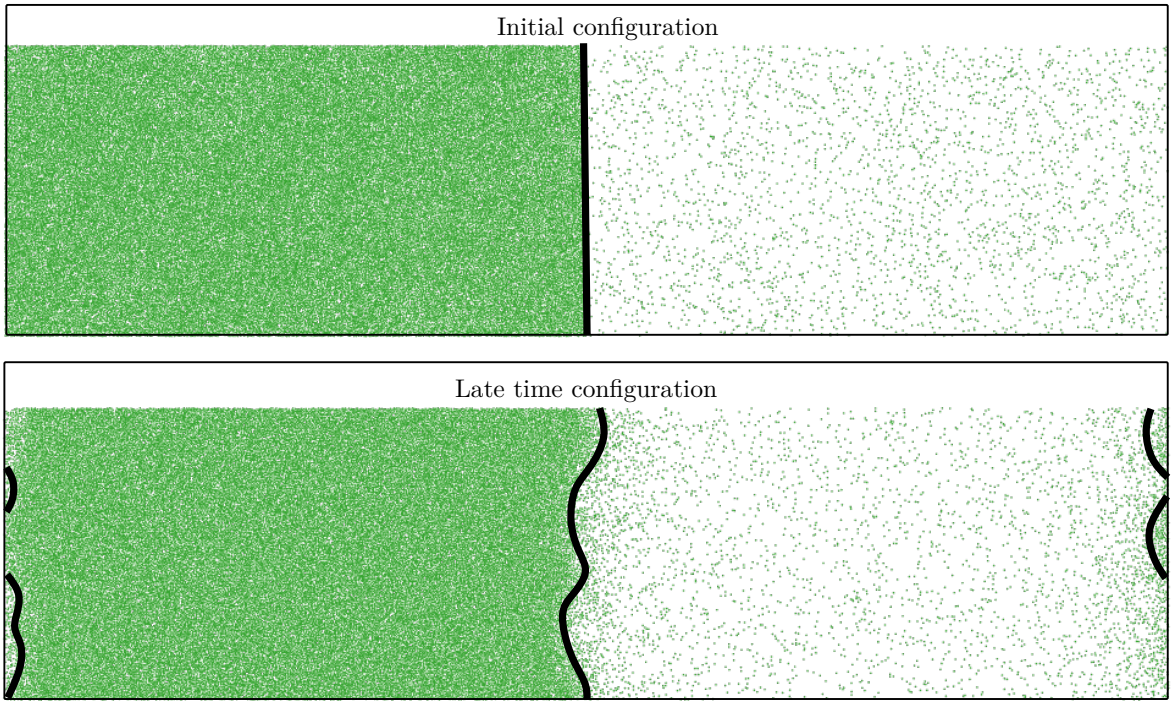

FIG. 1. Initial and late time configuration of a typical system.

We numerically integrate Eqs. (5) and (6) of the main text using an event-driven molecular dynamics algorithm [1], modified to include a Langevin bath via discrete-time kicks.

For simplicity, we first consider the case $T = 0$. In this regime, two particles i and j collide after a time:

$$\delta\tau_{ij}^{\text{coll}} = -\log\left(1 - \Gamma\delta\tau_{ij}\right)/\Gamma \quad \text{with} \quad \delta\tau_{ij} = \frac{-b - \sqrt{b^2 - \boldsymbol{v}_{ij}^2(\boldsymbol{r}_{ij}^2 - (\sigma_i + \sigma_j)^2/4)}}{\boldsymbol{v}_{ij}^2}, \tag{1}$$

where $b = \boldsymbol{r}_{ij} \cdot \boldsymbol{v}_{ij}$ and $\boldsymbol{r}_{ij} = \mathbf{r}_i - \mathbf{r}_j$ and $\boldsymbol{v}_{ij} = \boldsymbol{v}_i - \boldsymbol{v}_j$ are respectively the relative position and velocity of particles i and j at the moment the subsequent collision time is computed. σ_i is the diameter of particle i and $\delta\tau_{ij}$ is the collision time between two particles when $\Gamma \to 0$.

At each collision, particle velocities are updated according to the energy change given in Eq. (6) of the main text, leading to the post-collision velocities $\boldsymbol{v}'$:

$$\boldsymbol{v}_i' = \boldsymbol{v}_i - \frac{\boldsymbol{v}_{ij} \cdot \hat{\boldsymbol{\sigma}}_{ij} - \sqrt{\alpha^2(\boldsymbol{v}_{ij} \cdot \hat{\boldsymbol{\sigma}}_{ij})^2 + 4\Delta E^+/m}}{2}\hat{\boldsymbol{\sigma}}_{ij} \quad \text{and} \quad \boldsymbol{v}_j' = \boldsymbol{v}_j + \frac{\boldsymbol{v}_{ij} \cdot \hat{\boldsymbol{\sigma}}_{ij} - \sqrt{\alpha^2(\boldsymbol{v}_{ij} \cdot \hat{\boldsymbol{\sigma}}_{ij})^2 + 4\Delta E^+/m}}{2}\hat{\boldsymbol{\sigma}}_{ij}, \tag{2}$$

with $\hat{\boldsymbol{\sigma}}_{ij} = (\boldsymbol{r}_i - \boldsymbol{r}_j)/|\boldsymbol{r}_i - \boldsymbol{r}_j|$. A collision occurs only when particles are approaching one another, i.e., when $\boldsymbol{v}_{ij} \cdot \hat{\boldsymbol{\sigma}}_{ij} < 0$. Moreover, provided that $\Delta E^+ \geq 0$ and $\alpha > 0$, the collision rule guarantees that $\boldsymbol{v}_{ij}' \cdot \hat{\boldsymbol{\sigma}}_{ij} > 0$. Therefore, after the collision, the particles move apart along the line of centers, preventing any overlap.

For a binary mixture, the same collision rule holds except that they collide at $|\boldsymbol{r}_i - \boldsymbol{r}_j| = (\sigma_i + \sigma_j)/2$, as indicated in Eq. (1).

For $T \neq 0$, each particle receives stochastic kicks every δt_{noise}, drawn from a Gaussian distribution of variance $2\Gamma T \delta t_{\text{noise}}/m$ [2]. To properly resolve the dynamics, we require $\delta t_{\text{noise}} \ll \tau^{\text{coll}}$, where τ^{coll} is the mean free flight time between successive collisions.

For each parameter set, we first performed preliminary simulations in an elongated box to determine the coexistence densities. We initialized two half-box slabs at trial packing fractions, yielding an initially flat interface with a density field

$$\phi_{t=0}(x,y) \simeq \left(\phi_{\text{dense}}^{\text{coexistence}} - \phi_{\text{dilute}}^{\text{coexistence}}\right)\Theta(x - L_x/2) + \phi_{\text{dilute}}^{\text{coexistence}}, \tag{3}$$

where Θ is the Heaviside function. Both phases were seeded from independent amorphous configurations prepared by starting from a dilute system, and growing the particles until the target density is reached [1]. We then evolved the combined system until the bulk densities on each side reached stationary values. These densities (and the corresponding phases) were recorded, and we ran a short additional simulation initialized at the measured coexistence values to verify that the interface remained close to $x = L_x/2$, i.e., that the system lies near the center of the coexistence region. If not, we updated the trial densities and repeated until convergence, which fixes the total packing fraction $\phi = \pi\sigma^2 N/(4L_xL_y)$. Due to strong finite-size effects, the coexistence densities depend on system size and must be tuned for each L_x, L_y. During these runs, we also monitored whether the dense phase underwent a phase change: when large hexagonal domains formed, we classified the phase as solid-like.

Final production runs were then started by initializing, at $t = 0$, a flat interface using the converged homogeneous coexistence densities. The phases were initialized in their previously identified states (solid-like or liquid), except for $\delta E_0/\hat{E} = 0.0045$ in Fig. 2, where the dense phase was initialized as a liquid and slowly developed hexagonal patches for $t > 0$. We keep this as an instructive example, showing that a system with multiple hexatic domains behaves similarly to one with a single well-defined orientation.

When a solid-like initialization is required, we start from a perfect hexagonal lattice, which relaxes either to a solid with long-range orientational order or to a hexatic phase with quasi-long-range order, both with defects. While the steady state is insensitive to this initial relaxation, early-time coarsening may be affected.

The one-dimensional interface profile $h(y)$ is obtained by extracting the local packing fraction field $\phi(x,y)$ through binning via squares of length 5σ. The position of the interface $h(y)$ is placed by fitting each y-slice to a hyperbolic tangent: $\phi(x,y) = A\tanh[(x - h(y))/B] + C$. The interface coarsens with time and reaches a stationary regime at a time τ_{ss}, which is numerically obtained by looking at the intersection time between the early time power law of $W^2(L,t)$ and its stationary value $W^2(L, t \to \infty)$.

The initial and late time states of a typical system are illustrated in Fig. 1.

LARGE FINITE SIZE EFFECT WITH $\Gamma = 0$ AND DENSITY OSCILLATIONS

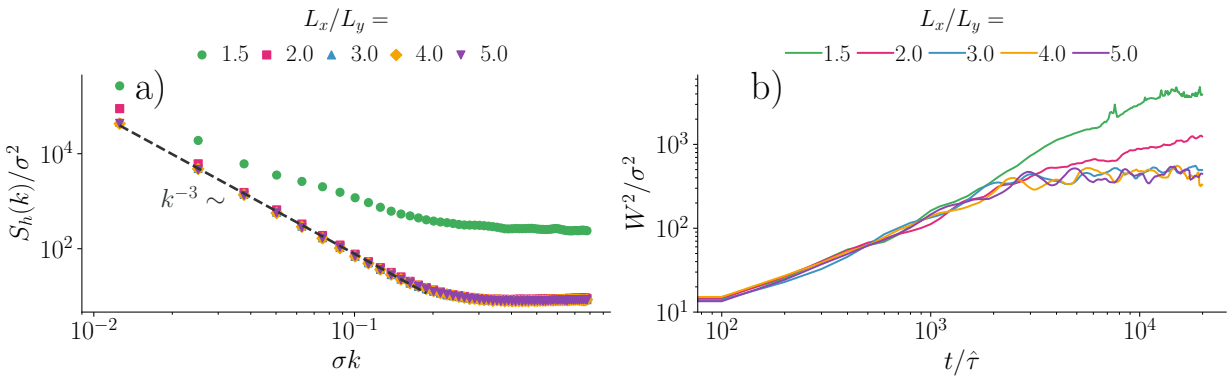

FIG. 2. Quantification of the finite size effects for the system with $\Gamma = 0$ and $L_y = 500\sigma$. a) Static height correlation function for various system sizes. b) Coarsening of these different system sizes with time. The parameters are the same as those used in Fig. 1 of the main text for the system with $\Gamma = 0$.

To isolate bulk-driven interfacial fluctuations, the simulation box must be sufficiently long in the direction perpendicular to the interface [3], ensuring that the two interfaces do not interact. For systems with $\Gamma = 0$, finite-size

effects become particularly severe. As shown in Fig. 2a) where L_x is varied for a fixed $L \equiv L_y$. S_h varies significantly for $L_x < 3L_y$. Correspondingly, Fig. 2b) shows anomalous coarsening dynamics in such undersized systems, with the interface roughness growing faster than in the largest system sizes. This issue worsens with increasing L_y as the critical aspect ratio L_x/L_y required to suppress finite-size artifacts also increases. Thus, larger interfaces demand even more elongated simulation boxes to reach the scaling regime. This result is perhaps not unexpected, as $\chi = 1$ marks the stability limit for an interface in the thermodynamic limit. Indeed, given the scaling $\sqrt{W_{ss}^2(L_y)} \sim L_y^{\chi}$, $\chi = 1$ implies the interface width increases proportionally to its base length. Consequently, for $\chi = 1+\varepsilon$ (with $\varepsilon > 0$), the interface becomes unstable for a given $L_y = L_y'$ such that $\sqrt{W^2(L_y')} > L_x$, if the aspect ratio L_x/L_y is held fixed.

However, increasing L_x introduces two complications: the simulation time strongly increases and standing waves emerge. Indeed, Fig. 3a) reveals oscillations in the mean interface width, which become increasingly prominent with system size. These oscillations correspond to standing compressive waves in the density field, as shown in Fig. 3b.) They originate from the mismatch between our initial condition—a sharp flat interface—and the smooth mechanical equilibrium profile expected due to surface tension, which resembles a $\tanh(x/\zeta)$ interpolation between bulk phases. The resulting force imbalance at the phase boundaries launches compressive waves that decay only weakly in the absence of external damping ($\Gamma = 0$).

This effect appears negligible for interfaces involving solid or glassy phases. Nevertheless, for gas-liquid systems, these density waves dominate interfacial coarsening, masking the intrinsic scaling behavior at early time and making it impossible to extract z. The examples provided here are exaggerated by purposely initializing the density field with a relatively large density mismatch compared to the measured coexistence densities.

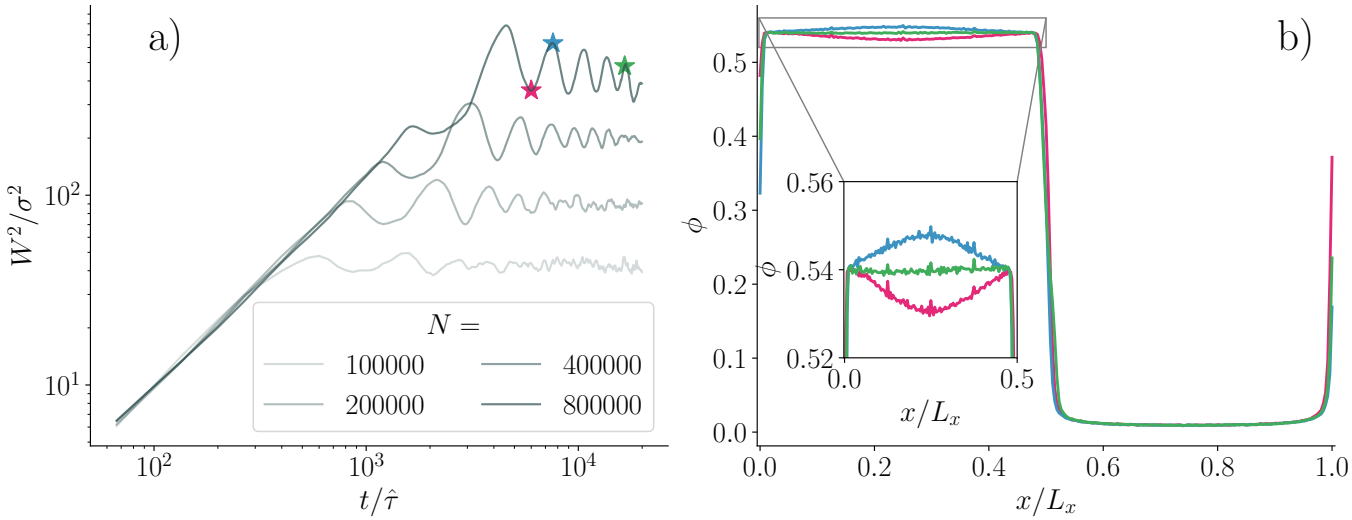

FIG. 3. Spurious oscillations due to initial force imbalance at the boundaries. a) Coarsening with respect to time for different system sizes. b) Density profile along the direction perpendicular to the interface at different times corresponding to the stars marked in a). The parameters are the same as those used in Fig. 1 of the main text for the system with $\Gamma = 0$.

COARSENING OF LIQUID-SOLID INTERFACES

Coarsening dynamics in systems undergoing liquid-solid phase separation are significantly more challenging to characterize than in liquid-gas systems. An accurate initialization is important: the solid phase should ideally be unstrained, for instance, using a direct-coexistence protocol [4]. In this work, we did not implement such equilibration procedures, which may affect quantitative details of the observed coarsening. Nonetheless, we report here the qualitative trends across the different systems studied in the main text.

We first consider how coarsening changes as parameters are varied to induce a structural change in the dense phase.

The most pronounced changes are observed for $\Gamma = 0$, shown in Fig. 4a). For large δE_0, the system remains in a liquid-gas regime and exhibits coarsening behavior similar to that discussed in the main text (note that we did not take any precaution to partially eliminate the spurious standing waves). As δE_0 is decreased, the dense phase begins to undergo a phase change. Intermediate values produce systems with multiple hexatic domains that coarsen over time, as the initial state was roughly a disordered fluid at the same density. Interestingly, $W^2(t)$ becomes non-monotonic:

the early-time increase corresponds to a predominantly liquid-gas interface, while the subsequent decrease reflects the formation of large hexatic domains that suppress interfacial fluctuations. We note that the W^2 becomes roughly constant at large time while the hexatic domains are still present and coarsening. We conclude that they coarsen slowly compared to the interface fluctuations. Further reduction of δE_0 yields a fully solid dense phase with markedly slower coarsening. For these systems, the dense phase was initialized with an ideal hexagonal solid.

In Fig. 4b), we provide the same figure but for the system following $|\boldsymbol{q}|$KPZ for the liquid-gas. Once again, ordering leads to a significantly reduced interface width. However, the coarsening phase at early time remains similar.

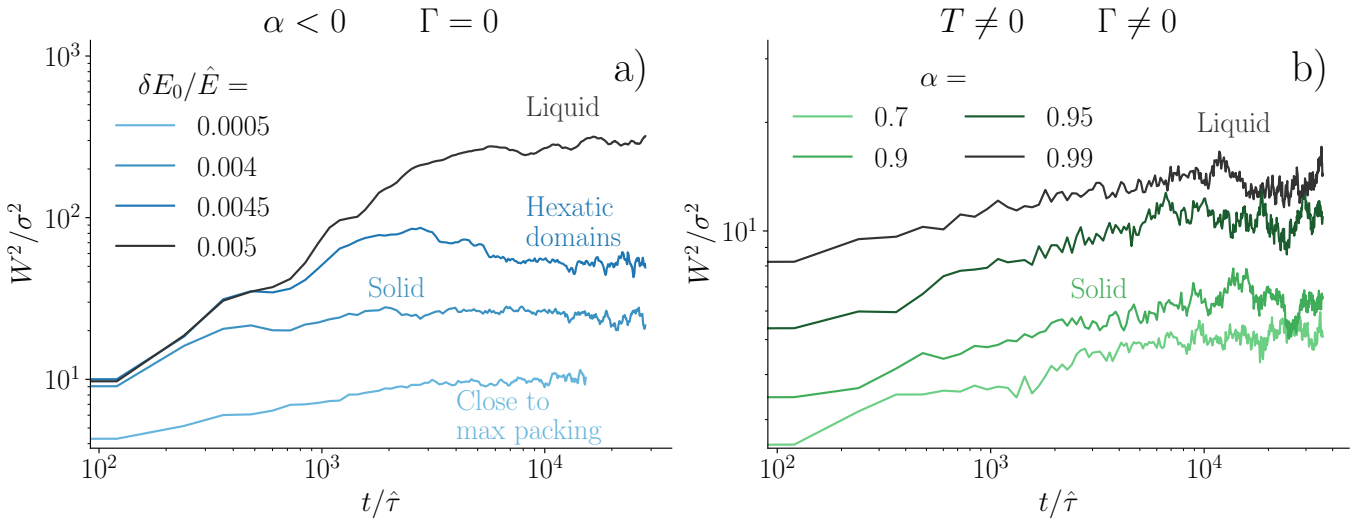

FIG. 4. Variation of the coarsening when the system changes from a liquid-gas to a liquid-solid phase separation. Left is a system with momentum conservation, right is without momentum conservation. The parameters are the same as those used in Fig. 2.

We now perform a finite-size analysis of systems with the smallest values of the control parameter, corresponding to the most densely packed solids. We first consider the system with $\Gamma = 0$ (left-hand side of Fig. 5). As shown in Fig. 5a) and c), the interface coarsens in a manner that prohibits a clear extraction of z. The steady state W^2 can, however, be extracted and is given in panel b). The approximate logarithmic scaling suggests $\chi \simeq 0$. This trend is consistent with the height structure factor $S_h(k)$ shown in panel d), which predicts $0 \lesssim \chi \lesssim 0.15$.

In contrast, the system with $\Gamma \neq 0$ (right-hand side of the figure) shows more regular behavior. As seen in panel e), the coarsening appears well-behaved, and analysis of panels f) and g) yields estimates of $0 \lesssim \chi \lesssim 0.1$ and $z \simeq 2.25$.

* raphael.maire@universite-paris-saclay.fr
† giuseppe.foffi@universite-paris-saclay.fr

[1] F. Smallenburg, Efficient event-driven simulations of hard spheres, Eur. Phys. J. E **45**, 22 (2022).
[2] L. Ma, X. Li, and C. Liu, Fluctuation-dissipation theorem consistent approximation of the langevin dynamics model, Commun. Math. Sci. **15**, 1171 (2017).
[3] M. Grant and R. C. Desai, Fluctuating hydrodynamics and capillary waves, Phys. Rev. A **27**, 2577 (1983).
[4] F. Smallenburg, G. Del Monte, M. de Jager, and L. Filion, A simple and accurate method to determine fluid–crystal phase boundaries from direct coexistence simulations, J. Chem. Phys. **160** (2024).

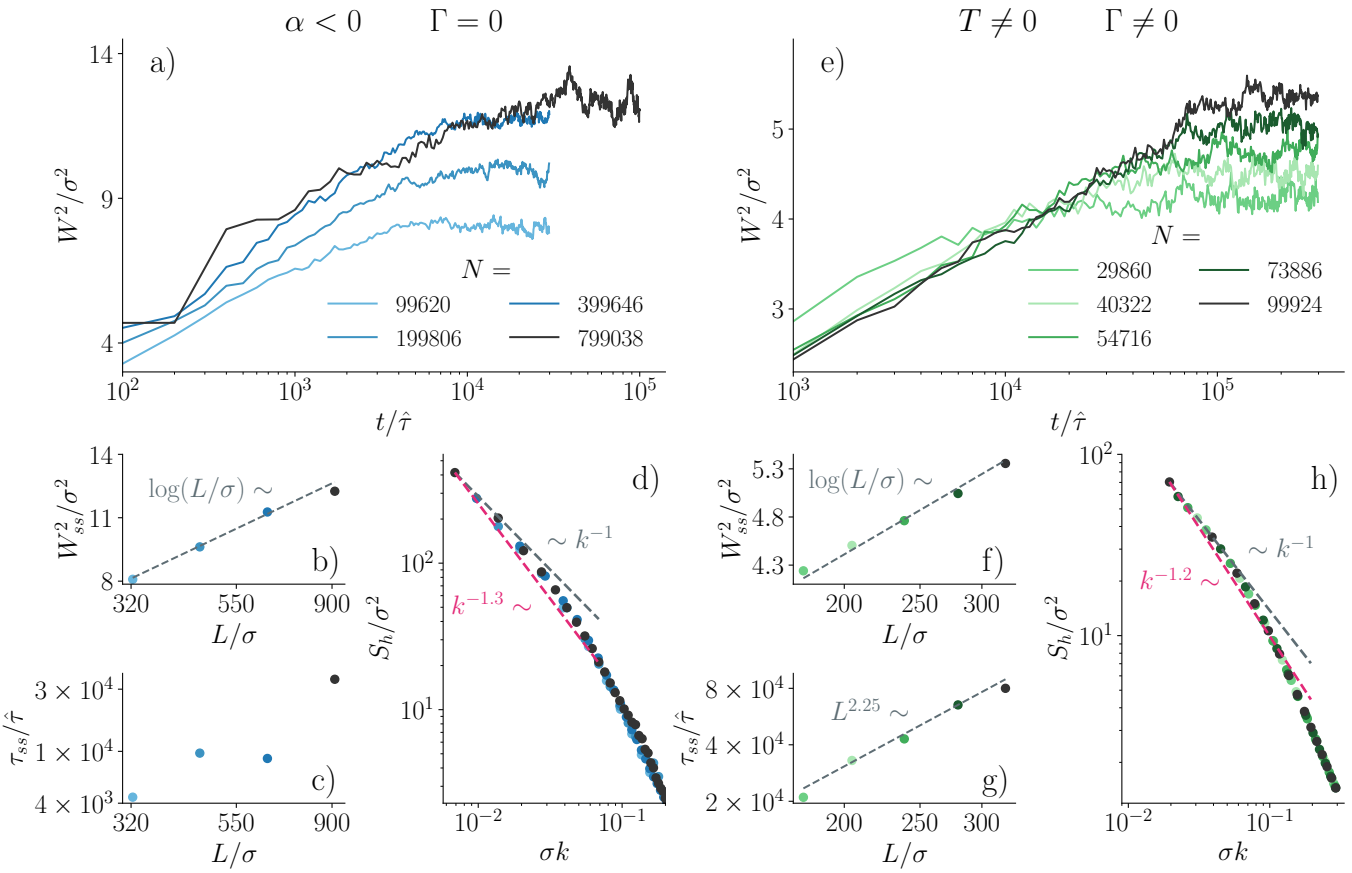

FIG. 5. Finite size analysis for the systems with a liquid-solid phase separation. The left panels correspond to systems with momentum conservation, while the right panels correspond to systems without momentum conservation. a) and e) are the evolution of the mean width squared as a function of time. b) and f) are the stationary values of W^2 as a function of L. c) and g) are the time required to reach this steady state value. d) and h) are the static height correlation in the steady state. For both systems, the parameters are the same as those used in Fig. 2, which lead to the densest glassy phase.